

SGS-3D: High-Fidelity 3D Instance Segmentation via Reliable Semantic Mask Splitting and Growing

Chaolei Wang¹, Yang Luo¹, Jing Du^{2*}, Siyu Chen^{3*}, Yiping Chen^{1†}, Ting Han^{1†}

¹Sun Yat-sen University ²University of Waterloo ³University of Glasgow

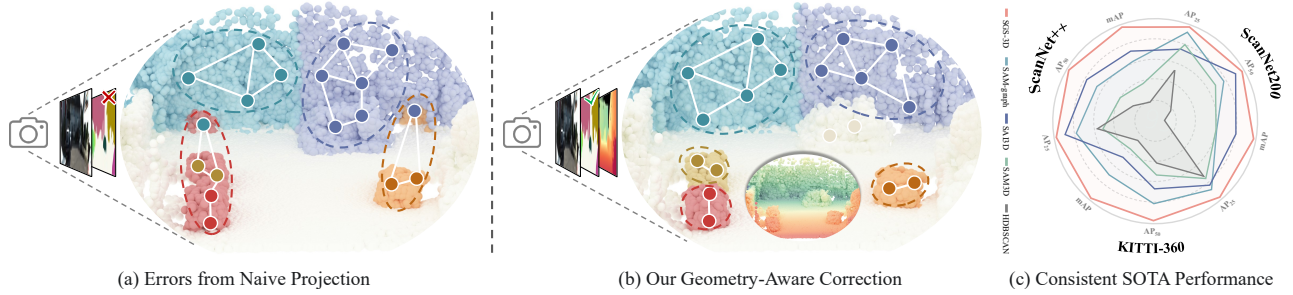


Figure 1: SGS-3D: High-Fidelity segmentation by overcoming ambiguous 2D-to-3D lifting. Previous methods suffer from flawed instance grouping (a), caused by ambiguous 2D semantics and inadequately unhandled occlusions during projection. SGS-3D overcomes this by establishing reliable 3D semantics via occlusion-aware mapping and a novel ”split-then-grow” refinement (b). This dual-refinement strategy achieves state-of-the-art accuracy across diverse scenes, especially in challenging, depth-less outdoor environments (c).

Abstract

Accurate 3D instance segmentation is crucial for high-quality scene understanding in the 3D vision domain. However, 3D instance segmentation based on 2D-to-3D lifting approaches struggle to produce precise instance-level segmentation, due to accumulated errors introduced during the lifting process from ambiguous semantic guidance and insufficient depth constraints. To tackle these challenges, we propose **Splitting and Growing** reliable **Semantic** mask for high-fidelity 3D instance segmentation (SGS-3D), a novel ”split-then-grow” framework that first purifies and splits ambiguous lifted masks using geometric primitives, and then grows them into complete instances within the scene. Unlike existing approaches that directly rely on raw lifted masks and sacrifice segmentation accuracy, SGS-3D serves as a training-free refinement method that jointly fuses semantic and geometric information, enabling effective cooperation between the two levels of representation. Specifically, for semantic guidance, we introduce a mask filtering strategy that leverages the co-occurrence of 3D geometry primitives to identify and remove ambiguous masks, thereby ensuring more reliable semantic consistency with the 3D object instances. For the geometric refinement, we construct fine-grained object instances by exploiting both spatial continuity and high-level features, particularly in the case of semantic ambiguity between distinct objects. Experimental results on ScanNet200, ScanNet++, and KITTI-360 demonstrate that SGS-3D substantially improves segmentation accuracy and robustness against inaccurate masks from pre-trained models, yielding high-fidelity object instances while maintaining strong generalization across diverse indoor and outdoor environments. Code is available in the supplementary materials.

Introduction

Arbitrary instances segmentation within 3D scenes constitutes a crucial task in various domains, including autonomous driving, virtual reality, and multi-modality scene understanding. While recent methods (Chen et al. 2021; Vu et al. 2022; Liang et al. 2021; Engelmann et al. 2020; Lu et al. 2023a; Schult et al. 2023) yield impressive segmentation results when trained on specifically annotated datasets (Dai et al. 2017; Armeni et al. 2016; Robert, Raguet, and Landrieu 2023; Yeshwanth et al. 2023; Liao, Xie, and Geiger 2022), their generalization to open-world environments remains limited. In contrast to the inherent difficulties in obtaining extensive 3D annotations, foundation models trained on massive 2D image datasets have shown remarkable performance and strong zero-shot generalization abilities. This observation motivates a promising direction: *utilizing 2D pre-trained foundation models for 3D scene perception and interaction*.

Currently, two predominant paradigms exist for executing the 3D instance segmentation: feature-based methods and mask-based methods. Feature-based methods (Peng et al. 2023; Takmaz et al. 2023; Xu et al. 2024; Lee, Zhao, and Lee 2024) primarily focus on learning robust feature representations from 3D point clouds or by lifting features from 2D modalities. Instance segmentation is subsequently achieved by classifying, grouping, or decoding these learned features into instance-level masks. However, these methods commonly suffer from inefficient training and error propagation, which arising from ambiguous feature representa-

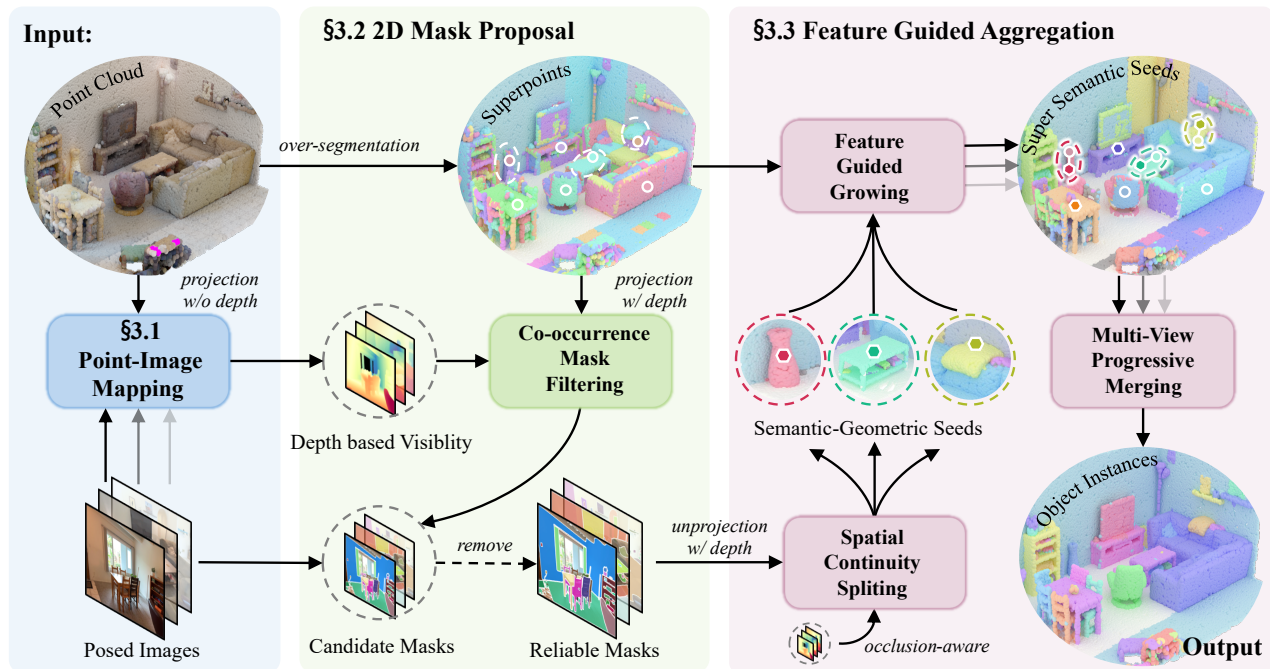


Figure 2: Overview of the training-free SGS-3D pipeline. Our method begins by computing robust, occlusion-aware point-image mappings without requiring ground-truth depth (§ 3.1). In the 2D Mask Proposal stage (§ 3.2), these mappings guide a Co-occurrence Mask Filtering process to prune ambiguous candidate masks, yielding a set of reliable 2D masks. These are then lifted to 3D and fed into the Feature-Guided Aggregation stage (§ 3.3), which first uses Spatial Continuity Splitting to generate pure semantic-geometric seeds. Subsequently, Feature-Guided Growing expands these seeds into complete instances, which are finally consolidated via Multi-View Progressive Merging to produce the final, high-fidelity object instances.

tions stemming from 2D-to-3D lifting or the inherent high-dimensional feature space.

To mitigate these concerns, mask-based methods leverage the semantic masks extracted from input registered images using Segment Anything Model (SAM) (Kirillov et al. 2023) to derive instance-level assignments for each 3D geometric primitive in the 3D scene, consolidating these 3D primitives iteratively based on their projected masks (Yang et al. 2023; Yin et al. 2024; Nguyen et al. 2024). Despite this advancement, the robust propagation of semantic information from these projected masks is often overlooked, with a primary focus on optimizing strategies for merging 3D geometric primitives while neglecting fine-grained geometric cues. This oversight leads to continuous error accumulation during scene segmentation, ultimately yielding imprecise results, particularly for adjacent but separate instances, as illustrated in Figure 1. Although some existing methods incorporate depth information from sensors to enhance back-projection accuracy (Guo et al. 2024; Yin et al. 2024), this reliance is problematic for two key reasons: depth sensors inherently struggle on textureless and highly reflective surfaces, and moreover, they are often entirely unavailable in wild scenes, severely compromising segmentation performance.

To confront these issues, we propose SGS-3D, a training-free refinement and segmentation framework that jointly fuse semantic and geometric information to accurately register 2D semantic instance masks to 3D geometric primitives.

Inspired by prior work, we introduce 3D geometric over-segmentation to decompose objects within the scene into primitives, which serve as the basic units for instance segmentation. Moreover, we reveal the significance of precise depth constraints, which serve as a powerful tool for propagating reliable and fine-grained semantic cues to 3D point clouds. Specifically, during the mask refinement phase, we first effectively establish a point-to-pixel mapping, without relying on true depth maps and without sacrificing precision. Leveraging this mapping, the co-occurrence of 3D geometric primitives effectively prevents the accumulation of ambiguous semantic errors. In the geometry refinement phase, we split 3D semantic masks within the density space to further refine semantic guidance and maintain semantic quality. After geometric optimization, our method consolidates the refined 3D semantic masks with geometric primitives by performing feature similarity matching, which enhances the completeness of object instances while reducing redundancy. To summarize our contributions in a few words:

- We propose SGS-3D, a novel training-free framework that achieves high-fidelity 3D instance segmentation through a principled “split-then-grow” strategy, jointly leveraging semantic and geometric cues to overcome error accumulation in existing 2D-to-3D lifting approaches.
- We introduce an occlusion-aware point-image mapping that ensures accurate mask-to-point correspondence without ground-truth depth, and develop a visibility-

based co-occurrence filtering mechanism that effectively removes ambiguous 2D masks while achieving $4\times$ computational speedup and robust cross-scene generalization.

- We design a semantic-guided aggregation pipeline featuring density-based spatial splitting to generate pure semantic-geometric seeds, followed by feature-guided growing that intelligently aggregates fragmented instances into complete objects, particularly excelling in challenging interwoven scenarios.

Methodology

Method Overview and Preliminaries

The proposed SGS-3D comprises three main components: (1) Point-Image Mapping, (2) 2D Mask Proposal Module, and (3) Semantic-Guided Aggregation, as illustrated in Figure 2. Our primary objective is to generate a set of high-quality, class-agnostic 3D instance proposals by leveraging semantic and spatial cues from multiple 2D views. Our method takes as input a 3D point cloud $P = \{p_i \in \mathbb{R}^6\}_{i=1}^N$ (XYZRGB) and a set of T registered images $\{I_t\}_{t=1}^T$ with their corresponding camera parameters, including intrinsics \mathbf{K}_t and pose \mathbf{T}_t .

We first over-segment the point cloud P into a set of U superpoints, $\mathcal{S} = \{s_u\}_{u=1}^U$, which serve as our fundamental processing primitives. These spatially coherent and geometrically compact groups of points improve computational efficiency and help maintain structural consistency. To adapt to diverse 3D scenarios, we employ method in (Dai et al. 2017) for indoor mesh inputs and (Robert, Raguét, and Landrieu 2023) for outdoor unstructured point clouds. Furthermore, for each superpoint s_u , we assume access to a pre-computed feature vector $\mathbf{f}_u \in \mathbb{R}^D$, derived from a pre-trained segmentation model (Schult et al. 2023), which captures its high-dimensional feature.

Point-Image Mapping

We start by establishing a robust and efficient mapping between the points in P and the images in I . A point-image pair (p, I_t) is considered compatible if the point p is visible in the image I_t . That is, p lies within the camera’s viewing frustum and is not occluded by any other point that is closer to the camera. For each compatible pair, we define its re-projection $\text{pix}(p, I_t)$ as the 2D pixel coordinate in image I_t where the point p is projected. However, computing this mapping is non-trivial, especially in multi-view scenarios where occlusions are common.

Depth Construction In contrast to existing methods that rely on ground-truth depth maps from dedicated sensors, we propose an efficient mapping strategy to compute visibility directly from the point cloud and camera parameters using Z-buffering (Ravi et al. 2020). For a given image I_t with its associated camera parameters $(\mathbf{K}_t, \mathbf{T}_t)$, the entire point cloud P is projected into the camera’s image plane. The transformation π maps a homogeneous world point p_i to pixel coordinates (u_i, v_i) with depth z_i , according to $z_i[u_i, v_i, 1]^T = \mathbf{K}_t \mathbf{T}_t^{-1} \mathbf{p}_i$. To resolve occlusions, a

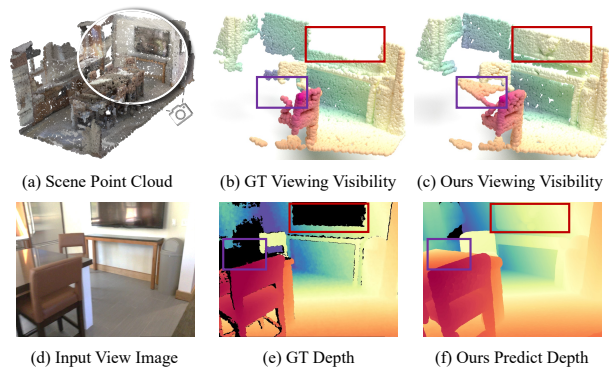


Figure 3: Our method constructs valid visibility mapping for each point. While depth sensors struggle on textureless and highly reflective surfaces, our approach remains effective.

depth buffer $\mathbf{D}_t \in \mathbb{R}^{H \times W}$ is initialized with infinite values. The final value at each pixel (u, v) is populated via a highly parallel rasterization process on the GPU, which efficiently solves for the minimum depth over the set of all points projecting to that location:

$$\mathbf{D}_t(u, v) = \min\{z_i \mid p_i \in P, \pi(p_i, \mathbf{K}_t, \mathbf{T}_t) = (u, v)\}. \quad (1)$$

Viewing Visibility Verification Subsequent to the generation of the metric depth buffer \mathbf{D}_t , we finalize the visibility status for each point. The per-point visibility for a view t is encapsulated in a binary tensor $\mathcal{V}_t \in \{0, 1\}^N$, whose elements are computed via a composite frustum and occlusion check:

$$\mathcal{V}_t(i) = \mathbf{1}(0 \leq u_i < W \wedge 0 \leq v_i < H) \cdot \mathbf{1}(|z_i - \mathbf{D}_t(u_i, v_i)| \leq \tau_{vis}), \quad (2)$$

where (u_i, v_i) and z_i are the projected pixel coordinates and true computed camera-space depth of point p_i , respectively, $\mathbf{1}(\cdot)$ is the indicator function, and τ_{vis} is the depth congruence tolerance. Simultaneously, we maintain a definitive point-to-pixel correspondence map $\mathcal{M}_{pix,t} \in \mathbb{Z}^{N \times 3}$, which stores the valid mapping $[u_i, v_i, 1]^T$ for each point where $\mathcal{V}_t(i) = 1$. This verification yields the precise, per-view mapping essential for subsequent sections, as illustrated in Figure 3.

2D Mask Proposal

Mask Generation Mask-based 3D instance segmentation involves generating masks for the target objects based on input images. For each image I_t in a scene sequence $I = \{I_t\}_{t=1}^T$, the objective is to produce a corresponding set of binary masks, $\mathcal{M}_{2D,t} = \{M_{t,k}\}_{k=1}^{K_t}$. With the emergence of foundational models like SAM (Kirillov et al. 2023), mask prediction has become highly precise. However, SAM lacks targeted guidance and often segments objects that are not of interest. Therefore, we apply Grounding-DINO (Liu et al. 2024) to extract box prompts from the images with text prompts. The high-confidence box prompts among them are then used to generate the initial mask predictions.

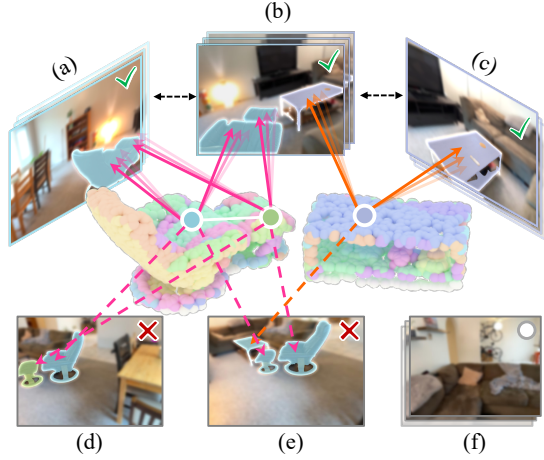


Figure 4: Co-occurrence mask filtering strategy. Co-occurrence scores between superpoints are constructed from accurate 2D mask sets (a-c). Over-segmented (d) and under-segmented (e) masks exhibiting low scores are then removed from the candidate masks list, where image sets with $\mathcal{P}_{vis,m}^j = 0$ (f) are excluded from the calculation.

Co-occurrence Mask Filtering Through introducing text prompts via Grounding-DINO, the number of semantically ambiguous masks should progressively decline. However, experiments reveal that although the quantity of major ambiguous masks reduces, some minor ambiguous ones still remain.

In fact, the binary masks $\mathcal{M}_{2D,t}$ predicted by the trained 2D vision foundation model exhibit discreteness, which often leads to inaccuracies and inconsistencies in object boundary area predictions across different views. This limitation may increase the instability of the semantic guidance of 2D masks. Unlike Maskclustering (Yan et al. 2024), which purely relies on image pixel consistency between views, we leverage viewing visibility of superpoints to exclusively enhance robustness against inaccurate masks.

Specifically, for superpoints belonging to the same instance, we accumulate their mutual visibility across multiple masks and views in Figure 4. We leverage our pre-computed point-to-pixel mappings $\mathcal{M}_{pix,t} \in \mathbb{Z}^{N \times 3}$ to establish the association between a superpoint and a 2D mask. A point p_i is considered to fall within a mask M_m in view j if it is physically visible ($\mathcal{V}_j(i) = 1$) and its projected pixel coordinates (u_i, v_i) lie inside the mask area. Let the set of all superpoints in the scene be $\mathcal{S} = \{s_u\}_{u=1}^U$. We define the association between a mask M_m and the superpoints it makes visible in view j , denoted as the set $\mathcal{P}_{vis,m}^j$:

$$\mathcal{P}_{vis,m}^j = \{s_u \in \mathcal{S} \mid \frac{|\{p_i \in s_u \mid \mathcal{V}_j(i)=1 \wedge M_m(\pi_j(p_i))=1\}|}{|s_u|} > 0.5\}. \quad (3)$$

Based on this, we define the visibility co-occurrence score c_m for each mask, which measures its average consistency with all other masks in the candidate set:

$$c_m = \frac{1}{(K_{2D} - 1)T} \sum_{n=1, n \neq m}^{K_{2D}} \sum_{j=1}^T \frac{|\mathcal{P}_{vis,m}^j \cap \mathcal{P}_{vis,n}^j|}{\sqrt{|\mathcal{P}_{vis,m}^j| \cdot |\mathcal{P}_{vis,n}^j|}}, \quad (4)$$

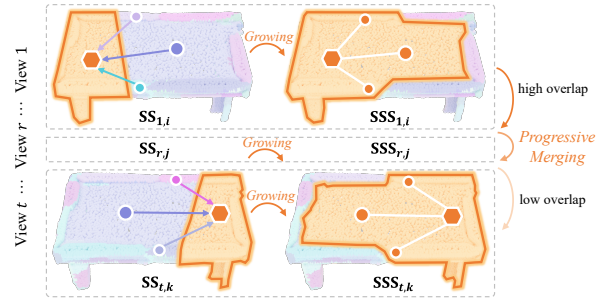


Figure 5: Semantic-guided aggregation. Within a single view, a Semantic-geometric Seed (SS) (orange) is expanded into a Super Semantic Seed (SSS) by merging with neighboring superpoints (colorful). Subsequently, these proposals from other views are progressively merged to form the final object instance.

where $\mathcal{P}_{vis,m}^j$ represents the set of visible superpoints for mask M_m in view j , T is the total number of views, and K_{2D} is the total number of masks in the candidate set. This principled score allows us to rank masks by their cross-view consistency. To prevent error propagation, masks exhibiting low co-occurrence scores, which indicate inconsistent visibility patterns, are identified as outliers and pruned from the candidate set.

Semantic-Guided Aggregation

Existing methods often compromise segmentation quality by either directly unprojecting 2D masks onto the point cloud (Yang et al. 2023; Yan et al. 2024) or by solely using them as a semantic prior to coarsely guide the iterative merging of superpoints (Yin et al. 2024; Nguyen et al. 2024). In such rough methods, the interplay between semantic and geometric information is not deeply exploited and leads to over-segmentation of object instances. To solve this problem, our unique insight is that leveraging reliable 3D semantics can enhance 3D segmentation and improve the robustness of instance aggregation.

Spatial Continuity Splitting Leveraging the occlusion-aware viewing visibility, we lift the filtered 2D masks from each view t onto point cloud. These point sets, aggregated by their shared semantic identity, are termed 3D semantic masks, $\mathcal{M}_{3D,t} = \{M_{t,k}\}_{k=1}^{K_t}$. While the 2D semantic consistency derived from vision models has proven effective in prior work, the intrinsic geometric coherence of the 3D point cloud itself is often overlooked. We experimentally find that objects with similar appearances are erroneously grouped into a single instance, despite being spatially distinct in the point cloud (see supplementary, Figure 10). As a solution, we apply HDBSCAN (Campello, Moulavi, and Sander 2013) on each of the 3D semantic masks ($M_{t,k} \in \mathcal{M}_{3D,t}$) which splits them into new clusters based on spatial contiguity. We refer to these dense clusters as semantic-geometric seeds, forming a new collection of fine-grained masks $\mathcal{M}_{seed,t} = \{M'_{t,j}\}_{j=1}^{K'_t}$. This density-based splitting utilizes geometric properties to refine the semantics of the segmentation results, ensuring a fine-grained distinction between instances and mitigating the propagation

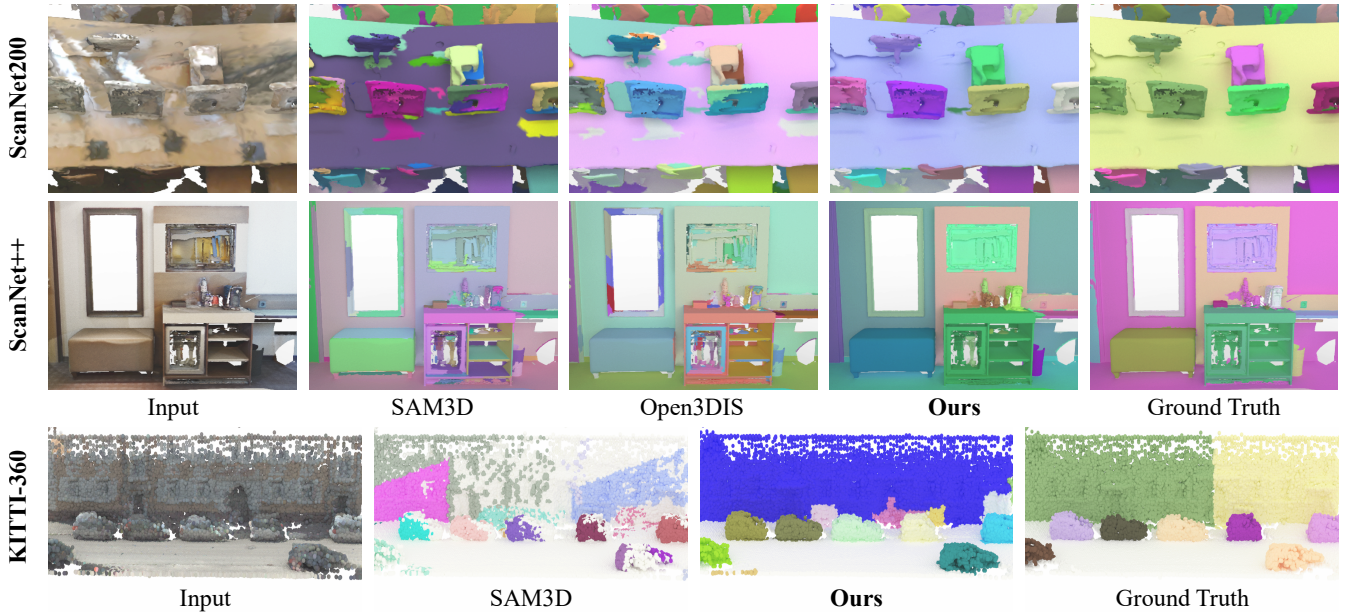


Figure 6: Qualitative comparison on indoor and outdoor datasets. Our method obtains more accurate segmentation results and significantly reduces over-segmentation or fragmented instances compared to previous method. For additional qualitative results, please refer to the supplementary materials.

of ambiguous semantics. The effectiveness of this geometric refinement in resolving semantic ambiguity is significant, as our ablation study shows it single-handedly surpasses existing state-of-the-art methods (see Table 2).

Single-View Feature-Guided Growing While the preceding density-based splitting excels at purifying seeds by enforcing geometric separation, producing $\mathcal{M}_{seed,t}$, it introduces a new challenge: how to correctly ensemble these over-segmented superpoints into complete object instances. To address this, we introduce a high-dimensional feature guided growing process. The core insight is to leverage the rich semantic context from pre-trained features (Schult et al. 2023), to intelligently bridge the spatial gaps between these semantic-geometric seeds and their corresponding object parts.

Rather than applying rigid thresholds, our growing process is guided by a unified affinity score that naturally balances semantic coherence with spatial adjacency, as illustrated in Figure 5. For a given seed $M'_{t,j} \in \mathcal{M}_{seed,t}$ and a candidate neighbor superpoint s_u , we define this score as:

$$\text{Affinity}(M'_{t,j}, s_u) = \text{sim}(\bar{\mathbf{f}}_{t,j}, \mathbf{f}_u) \cdot \text{Overlap}(M'_{t,j}, s_u), \quad (5)$$

where $\text{sim}(\bar{\mathbf{f}}_{t,j}, \mathbf{f}_u)$ is the cosine similarity between the seed’s mean feature and the candidate’s mean feature, and $\text{Overlap}(\cdot, \cdot)$ measures their spatial overlap, calculated as the intersection-over-union (IoU) of their 3D point sets. This multiplicative form ensures that a high affinity is only achieved when both semantic similarity and spatial overlap are strong.

At each step of the expansion, we identify the unassigned neighbor with the highest affinity score and merge it into the seed. This process continues iteratively, always selecting the most promising candidate, until the affinity scores of

all remaining neighbors become negligible, indicating that no more relevant parts can be found. By optimizing for the highest affinity, object instances can correctly associate disparate parts of the same object and expand its boundary, ready for the final aggregation stage.

Multi-View Progressive Merging The single-view growing process generates high-fidelity instance proposals, which are essentially the grown semantic-geometric seeds from $\mathcal{M}_{seed,t}$. However, each proposal is inherently limited to the information available from its originating viewpoint. To reconcile these partial views into complete objects, we employ a progressive, multi-view merging strategy. Inspired by (Yin et al. 2024), we initially merge proposals from different views only if their 3D spatial overlap is very high, ensuring only unambiguous matches are made. Subsequent iterations systematically relax this overlap requirement, allowing fragmented parts of the same large instance to be fused. This hierarchical process robustly assembles the final, complete 3D object instances for the entire scene, effectively consolidating information from multiple views.

Experiments

Experimental Setup

We evaluate our method on three prevalent 3D scene instance segmentation benchmarks: ScanNet200 (Dai et al. 2017), ScanNet++ (Yeshwanth et al. 2023) for indoor environments, and KITTI-360 (Liao, Xie, and Geiger 2022) for outdoor scenes. Following the evaluation protocols established in (Rozenberszki, Litany, and Dai 2024; Schult et al. 2023; Takmaz et al. 2023), we compute AP scores at 50% (AP_{50}) and 25% (AP_{25}) intersection-over-union (IoU) thresholds, as well as the mean AP (mAP) averaged over

Methods	Proc. & Year	VFM	ScanNet200			ScanNet++			KITTI-360		
			mAP	AP ₅₀	AP ₂₅	mAP	AP ₅₀	AP ₂₅	mAP	AP ₅₀	AP ₂₅
<i>training-dependent</i>											
UnScene3D	CVPR24	DINO	15.9	32.2	58.5	-	-	-	-	-	-
Segment3D	ECCV24	SAM	-	-	-	12.0	22.7	37.8	-	-	-
SAM-graph	ECCV24	SAM	22.1	41.7	<u>62.8</u>	15.3	27.2	44.3	<u>23.8</u>	<u>37.2</u>	<u>49.1</u>
<i>training-free</i>											
HDBSCAN	ICDMW17	-	2.9	8.2	33.1	4.3	10.6	32.3	9.3	18.9	39.6
Felzenszwalb	IJCV04	-	4.8	9.8	27.5	4.1	9.2	25.3	-	-	-
SAM3D	ICCVW23	SAM	20.9	34.8	51.4	9.3	16.6	29.5	13.0	24.2	41.1
Open3DIS	CVPR24	GD-SAM	29.7	45.2	56.8	18.5	35.5	44.3	-	-	-
SAI3D	CVPR24	SAM	28.2	<u>47.2</u>	48.5	17.1	31.1	49.5	16.5	30.2	45.6
SAM2Object	CVPR25	SAM2	-	-	-	20.2	34.1	48.7	-	-	-
Ours⁻	-	GD-SAM	<u>30.5</u>	<u>47.2</u>	62.2	<u>22.5</u>	<u>36.6</u>	<u>53.0</u>	32.9 _{+16.4}	43.7 _{+13.5}	53.4 _{+7.8}
Ours⁺	-	GD-SAM	34.3 _{+4.6}	51.3 _{+4.1}	64.6 _{+7.8}	23.7 _{+3.5}	39.6 _{+4.1}	54.3 _{+4.8}	-	-	-

Table 1: Quantitative results compared with conventional clustering methods and diverse 2D-to-3D lifting methods on ScanNet200, ScanNet++ and KITTI-360. "VFM" denotes the vision foundation models. Ours⁻ and Ours⁺ represent our method without and with ground-truth (GT) depth, respectively. All 2D-to-3D lifting baselines use GT depth. Best results are in **bold** (%), and the second-best are underlined.

50% to 95% IoU thresholds in 5% increments. Implementation details and more experiments are provided in supplementary material.

Analysis Experiments

Quantitative Results As shown in Table 1, SGS-3D achieves state-of-the-art performance among training-free methods across all benchmarks. The most striking result is on the challenging, depth-less KITTI-360 dataset, where Ours⁻ establishes a remarkable +16.4% mAP lead over the next best competitor, SAI3D. This validates the critical role of our occlusion-aware mapping in robust outdoor scene understanding. On indoor scenes, Ours⁻ also consistently surpasses previous SOTA methods, outperforming Open3DIS on ScanNet200 and SAM2Object on ScanNet++. Furthermore, when provided with GT depth, Ours⁺ sets a new performance ceiling. It achieves 34.3% mAP on ScanNet200 and 23.7% mAP on ScanNet++, outperforming all training-free baselines and even several training-dependent approaches, which showcases the strong potential of our refinement framework.

Qualitative Results As shown in Figure 6, our method produces visually superior results with more complete and geometrically precise instances. This enhanced quality stems directly from our framework’s ability to mitigate semantic ambiguity through robust mask filtering and spatial continuity splitting, leading to cleaner boundaries and more coherent object segmentation.

Ablation Study Table 2 details the contribution of each component. Co-occurrence Mask Filtering (CMF) first boosts mAP to 27.8% by refining initial mask semantics. A key insight comes from then adding Spatial Continuity Splitting (SCP); this variant, relying solely on our purified 3D masks without any superpoint-based growing, achieves an impressive 30.1% mAP. This result alone surpasses state-

of-the-art methods like SAM-graph (22.1% mAP), proving the power of our approach in resolving semantic ambiguity at its source. Finally, integrating Feature-Guided Growing (FGG) elevates performance to our full model’s 34.3% mAP, confirming a powerful synergy where our initial purification stages create high-quality seeds for FGG to complete (see Figure 7).

No.	CMF	SCP	FGG	mAP	AP ₅₀	AP ₂₅
1				25.9	41.9	57.3
2	✓			27.8	44.0	59.0
3	✓	✓		30.1	46.8	61.4
4	✓		✓	29.7	45.2	58.9
5	✓	✓	✓	34.3	51.3	64.6

Table 2: Ablation of the effectiveness of our proposed components. CMF indicates the co-occurrence mask filtering; SCP indicates the spatial continuity Splitting; FGG indicates the feature-guided growing.

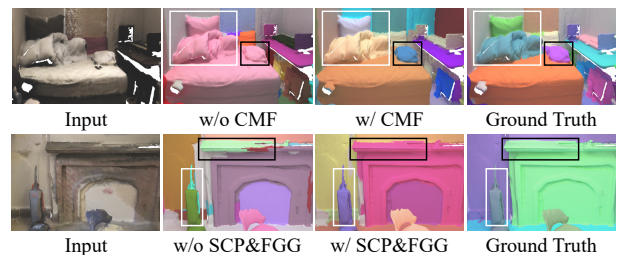


Figure 7: Ablation visualization results. Top: 2D mask proposal section; Bottom: semantic-guided aggregation section.

Efficiency and Robustness Table 4 highlights SGS-3D’s exceptional efficiency and accuracy. Most notably, our method achieves superior accuracy to Open3DIS while using only a quarter of the images (2.5% vs. 10%) and be-

Methods	Proc. & Year	3D Mask	mAP	AP ₅₀	AP ₂₅	mAP _{head}	mAP _{common}	mAP _{tail}
OpenMask3D	NeurIPS23	Supervised	15.4	19.9	23.1	17.1	14.1	14.9
OVIR-3D	CoRL23	Zero-shot	9.3	18.7	<u>25.0</u>	-	-	-
SAM3D	ICCVW23	Zero-shot	9.8	15.2	20.7	9.2	8.3	12.3
SAI3D	CVPR24	Zero-shot	12.7	18.8	24.1	<u>12.1</u>	<u>10.4</u>	<u>16.2</u>
SAM2Object	CVPR25	Zero-shot	<u>13.3</u>	<u>19.0</u>	23.8	-	-	-
Ours	-	Zero-shot	21.1 _{+7.8}	29.4 _{+10.4}	35.0 _{+10.0}	21.6 _{+9.5}	20.0 _{+9.6}	22.0 _{+5.8}

Table 3: Semantic results on ScanNet200. Head, common, and tail categories represent object classes with high, medium, and low frequencies in the dataset, respectively. OpenMask3D (Takmaz et al. 2023) requires supervised training on ScanNet200. In fully zero-shot setting, our method surpass previous SOTA methods by a large margin on all metrics.

Method	Img. Prop.	mAP	AP ₅₀	AP ₇₅	Time	Inst. Pred.
Open3DIS	10%	29.7	45.2	56.8	9.18s	102
Ours	10%	34.3	51.3	64.6	9.51s	62
	5%	33.7	51.1	64.5	4.94s	66
	2.5%	31.8	48.8	63.2	2.42s	68

Table 4: Influence of input image proportion on segmentation efficiency and performance. Inst. Pred. indicates predicted instance counts per scene.

VFM	mAP	AP ₅₀	AP ₂₅	c_m	mAP	AP ₅₀	AP ₂₅
Cropformer	33.6	50.7	63.1	0.4	33.8	50.2	63.1
SAM	32.3	47.8	<u>63.8</u>	0.3	34.0	50.9	63.2
YoloW-SAM	32.4	49.5	62.3	0.2	34.3	51.6	64.6
GD-SAM	34.3	51.3	64.6	0.1	32.0	48.3	61.8

Table 5: Ablation of different 2D vision models.

ing nearly four times faster. This underscores the remarkable data efficiency and computational performance of our approach. When provided with the same image proportion, SGS-3D’s accuracy advantage widens significantly. This performance gain is also reflected in proposal quality; our method dramatically reduces over-segmentation, cutting the number of predicted instances by nearly 40% compared to Open3DIS (62 vs. 102).

We further evaluated diverse vision foundation models (VFMs, e.g., Cropformer (Qi et al. 2022) and YoloWorld-SAM (Cheng et al. 2024)) to provide initial mask proposals, as shown in Table 5. Our pipeline consistently performs well across different models, demonstrating its robustness. As shown in Table 6, we evaluated the sensitivity of our co-occurrence filtering to the score threshold c_m . The performance remains stable across a range of values, with the optimal result achieved at 0.2, which we use as our default.

Percentage	0	5	10	30	50	60	70	90
mAP	34.3	34.1	34.1	33.4	29.6	24.2	14.8	0.1

Table 7: Robustness to simulated occlusion.

Moreover, we evaluate SGS-3D robustness to occlusion using the patch-drop protocol from (Naseer et al. 2021). Table 7 shows that our method remains highly resilient, main-



Figure 8: Open-vocabulary 3D object search. Given a text prompt, our method can accurately locate the corresponding object instances (pink) in a 3D scene, even for rare or uncommon object categories.

taining competitive performance even when up to 50% of the key foreground masks are occluded. Performance degrades gracefully under more severe occlusion, confirming the stability of our pipeline.

Open-Set Scene Understanding Application

The high-quality, class-agnostic instance proposals generated by SGS-3D serve as a powerful foundation for open-set scene understanding. By simply assigning semantic labels to our proposals using an off-the-shelf vision-language model (Zhai et al. 2023), our method can be seamlessly extended to open-vocabulary 3D segmentation (details in supplementary). As shown in Table 3, SGS-3D’s superior performance stems directly from our model’s ability to produce geometrically precise and complete instance masks, which prevents semantic ambiguity and ensures accurate label assignment. This capability enables robust, real-world applications such as interactive, text-based object search within complex 3D environments, as illustrated in Figure 8.

Conclusion

We have presented SGS-3D, a training-free framework that achieves high-fidelity 3D instance segmentation by resolving key limitations in 2D-to-3D lifting. Our method introduces a “split-then-grow” strategy: we first leverage geometric co-occurrence and spatial continuity to filter and split noisy semantic proposals into pure seeds, then use a feature-guided process to grow these seeds into complete and accurate instances. Extensive experiments on ScanNet200, ScanNet++, and KITTI-360 show that SGS-3D substantially outperforms state-of-the-art methods, even without relying on ground-truth depth. By creating a more robust bridge between 2D semantics and 3D geometry, our work provides a powerful foundation for class-agnostic segmentation and

downstream open-set tasks. Future directions include extending our framework to dynamic scenes by incorporating temporal information and optimizing its multi-stage design for real-time performance.

References

- Armeni, I.; Sener, O.; Zamir, A. R.; Jiang, H.; Brilakis, I.; Fischer, M.; and Savarese, S. 2016. 3d semantic parsing of large-scale indoor spaces. In *Proceedings of the IEEE conference on computer vision and pattern recognition*, 1534–1543.
- Boudjoghra, M. E. A.; Dai, A.; Lahoud, J.; Cholakkal, H.; Anwer, R. M.; Khan, S.; and Khan, F. S. 2024. Open-yolo 3d: Towards fast and accurate open-vocabulary 3d instance segmentation. *arXiv preprint arXiv:2406.02548*.
- Campello, R. J.; Moulavi, D.; and Sander, J. 2013. Density-based clustering based on hierarchical density estimates. In *Pacific-Asia conference on knowledge discovery and data mining*, 160–172. Springer.
- Chen, S.; Fang, J.; Zhang, Q.; Liu, W.; and Wang, X. 2021. Hierarchical aggregation for 3d instance segmentation. In *Proceedings of the IEEE/CVF International Conference on Computer Vision*, 15467–15476.
- Cheng, T.; Song, L.; Ge, Y.; Liu, W.; Wang, X.; and Shan, Y. 2024. Yolo-world: Real-time open-vocabulary object detection. In *Proceedings of the IEEE/CVF conference on computer vision and pattern recognition*, 16901–16911.
- Dai, A.; Chang, A. X.; Savva, M.; Halber, M.; Funkhouser, T.; and Nießner, M. 2017. Scannet: Richly-annotated 3d reconstructions of indoor scenes. In *Proceedings of the IEEE conference on computer vision and pattern recognition*, 5828–5839.
- Ding, R.; Yang, J.; Xue, C.; Zhang, W.; Bai, S.; and Qi, X. 2023. Pla: Language-driven open-vocabulary 3d scene understanding. In *Proceedings of the IEEE/CVF conference on computer vision and pattern recognition*, 7010–7019.
- Engelmann, F.; Bokeloh, M.; Fathi, A.; Leibe, B.; and Nießner, M. 2020. 3d-mpa: Multi-proposal aggregation for 3d semantic instance segmentation. In *Proceedings of the IEEE/CVF conference on computer vision and pattern recognition*, 9031–9040.
- Felzenszwalb, e. a. 2004. Efficient graph-based image segmentation. *International journal of computer vision*, 59: 167–181.
- Guo, H.; Zhu, H.; Peng, S.; Wang, Y.; Shen, Y.; Hu, R.; and Zhou, X. 2024. Sam-guided graph cut for 3d instance segmentation. In *European Conference on Computer Vision*, 234–251. Springer.
- Han, L.; Zheng, T.; Xu, L.; and Fang, L. 2020. Occuseg: Occupancy-aware 3d instance segmentation. In *Proceedings of the IEEE/CVF conference on computer vision and pattern recognition*, 2940–2949.
- Han, T.; Chen, Y.; Ma, J.; Liu, X.; Zhang, W.; Zhang, X.; and Wang, H. 2024. Point cloud semantic segmentation with adaptive spatial structure graph transformer. *International Journal of Applied Earth Observation and Geoinformation*, 133: 104105.
- He, T.; Shen, C.; and Van Den Hengel, A. 2021. Dyco3d: Robust instance segmentation of 3d point clouds through dynamic convolution. In *Proceedings of the IEEE/CVF conference on computer vision and pattern recognition*, 354–363.
- Hegde, D.; Valanarasu, J. M. J.; and Patel, V. 2023. Clip goes 3d: Leveraging prompt tuning for language grounded 3d recognition. In *Proceedings of the IEEE/CVF International Conference on Computer Vision*, 2028–2038.
- Hou, J.; Dai, A.; and Nießner, M. 2019. 3d-sis: 3d semantic instance segmentation of rgb-d scans. In *Proceedings of the IEEE/CVF conference on computer vision and pattern recognition*, 4421–4430.
- Huang, R.; Peng, S.; Takmaz, A.; Tombari, F.; Pollefeys, M.; Song, S.; Huang, G.; and Engelmann, F. 2024. Segment3d: Learning fine-grained class-agnostic 3d segmentation without manual labels. In *European Conference on Computer Vision*, 278–295. Springer.
- Jia, C.; Yang, Y.; Xia, Y.; Chen, Y.-T.; Parekh, Z.; Pham, H.; Le, Q.; Sung, Y.-H.; Li, Z.; and Duerig, T. 2021. Scaling up visual and vision-language representation learning with noisy text supervision. In *International conference on machine learning*, 4904–4916. PMLR.
- Jiang, L.; Zhao, H.; Shi, S.; Liu, S.; Fu, C.-W.; and Jia, J. 2020. Pointgroup: Dual-set point grouping for 3d instance segmentation. In *Proceedings of the IEEE/CVF conference on computer vision and Pattern recognition*, 4867–4876.
- Kirillov, A.; Mintun, E.; Ravi, N.; Mao, H.; Rolland, C.; Gustafson, L.; Xiao, T.; Whitehead, S.; Berg, A. C.; Lo, W.-Y.; et al. 2023. Segment anything. In *Proceedings of the IEEE/CVF international conference on computer vision*, 4015–4026.
- Kolodiazhnyi, M.; Vorontsova, A.; Konushin, A.; and Rukhovich, D. 2024. Top-down beats bottom-up in 3d instance segmentation. In *Proceedings of the IEEE/CVF Winter Conference on Applications of Computer Vision*, 3566–3574.
- Lai, X.; Liu, J.; Jiang, L.; Wang, L.; Zhao, H.; Liu, S.; Qi, X.; and Jia, J. 2022. Stratified transformer for 3d point cloud segmentation. In *Proceedings of the IEEE/CVF conference on computer vision and pattern recognition*, 8500–8509.
- Landrieu, L.; and Simonovsky, M. 2018. Large-scale point cloud semantic segmentation with superpoint graphs. In *Proceedings of the IEEE conference on computer vision and pattern recognition*, 4558–4567.
- Lee, S.; Zhao, Y.; and Lee, G. H. 2024. Segment any 3d object with language. *arXiv preprint arXiv:2404.02157*.
- Liang, Z.; Li, Z.; Xu, S.; Tan, M.; and Jia, K. 2021. Instance segmentation in 3d scenes using semantic superpoint tree networks. In *Proceedings of the IEEE/CVF international conference on computer vision*, 2783–2792.
- Liao, Y.; Xie, J.; and Geiger, A. 2022. Kitti-360: A novel dataset and benchmarks for urban scene understanding in 2d and 3d. *IEEE Transactions on Pattern Analysis and Machine Intelligence*, 45(3): 3292–3310.
- Liu, S.; Zeng, Z.; Ren, T.; Li, F.; Zhang, H.; Yang, J.; Jiang, Q.; Li, C.; Yang, J.; Su, H.; et al. 2024. Grounding dino:

- Marrying dino with grounded pre-training for open-set object detection. In *European Conference on Computer Vision*, 38–55. Springer.
- Lu, J.; Deng, J.; Wang, C.; He, J.; and Zhang, T. 2023a. Query refinement transformer for 3d instance segmentation. In *Proceedings of the IEEE/CVF International Conference on Computer Vision*, 18516–18526.
- Lu, S.; Chang, H.; Jing, E. P.; Boularias, A.; and Bekris, K. 2023b. Ovir-3d: Open-vocabulary 3d instance retrieval without training on 3d data. In *Conference on Robot Learning*, 1610–1620. PMLR.
- McInnes, L.; and Healy, J. 2017. Accelerated hierarchical density based clustering. In *2017 IEEE international conference on data mining workshops (ICDMW)*, 33–42. IEEE.
- Milioto, A.; Vizzo, I.; Behley, J.; and Stachniss, C. 2019. Rangenet++: Fast and accurate lidar semantic segmentation. In *2019 IEEE/RSJ international conference on intelligent robots and systems (IROS)*, 4213–4220. IEEE.
- Naseer, M. M.; Ranasinghe, K.; Khan, S. H.; Hayat, M.; Shahbaz Khan, F.; and Yang, M.-H. 2021. Intriguing properties of vision transformers. *Advances in Neural Information Processing Systems*, 34: 23296–23308.
- Ngo, T. D.; Hua, B.-S.; and Nguyen, K. 2023. Isbnet: a 3d point cloud instance segmentation network with instance-aware sampling and box-aware dynamic convolution. In *Proceedings of the IEEE/CVF Conference on Computer Vision and Pattern Recognition*, 13550–13559.
- Nguyen, P.; Ngo, T. D.; Kalogerakis, E.; Gan, C.; Tran, A.; Pham, C.; and Nguyen, K. 2024. Open3dis: Open-vocabulary 3d instance segmentation with 2d mask guidance. In *Proceedings of the IEEE/CVF Conference on Computer Vision and Pattern Recognition*, 4018–4028.
- Peng, S.; Genova, K.; Jiang, C.; Tagliasacchi, A.; Pollefeys, M.; Funkhouser, T.; et al. 2023. Openscene: 3d scene understanding with open vocabularies. In *Proceedings of the IEEE/CVF conference on computer vision and pattern recognition*, 815–824.
- Qi, C. R.; Su, H.; Mo, K.; and Guibas, L. J. 2017a. Pointnet: Deep learning on point sets for 3d classification and segmentation. In *Proceedings of the IEEE conference on computer vision and pattern recognition*, 652–660.
- Qi, C. R.; Yi, L.; Su, H.; and Guibas, L. J. 2017b. Pointnet++: Deep hierarchical feature learning on point sets in a metric space. *Advances in neural information processing systems*, 30.
- Qi, L.; Kuen, J.; Guo, W.; Shen, T.; Gu, J.; Jia, J.; Lin, Z.; and Yang, M.-H. 2022. High-quality entity segmentation. *arXiv preprint arXiv:2211.05776*.
- Qian, G.; Li, Y.; Peng, H.; Mai, J.; Hammoud, H.; Elhoseiny, M.; and Ghanem, B. 2022. Pointnext: Revisiting pointnet++ with improved training and scaling strategies. *Advances in neural information processing systems*, 35: 23192–23204.
- Radford, A.; Kim, J. W.; Hallacy, C.; Ramesh, A.; Goh, G.; Agarwal, S.; Sastry, G.; Askell, A.; Mishkin, P.; Clark, J.; et al. 2021. Learning transferable visual models from natural language supervision. In *International conference on machine learning*, 8748–8763. PmlR.
- Ravi, N.; Gabeur, V.; Hu, Y.-T.; Hu, R.; Ryali, C.; Ma, T.; Khedr, H.; Rädle, R.; Rolland, C.; Gustafson, L.; et al. 2024. Sam 2: Segment anything in images and videos. *arXiv preprint arXiv:2408.00714*.
- Ravi, N.; Reizenstein, J.; Novotny, D.; Gordon, T.; Lo, W.-Y.; Johnson, J.; and Gkioxari, G. 2020. Accelerating 3d deep learning with pytorch3d. *arXiv preprint arXiv:2007.08501*.
- Ren, T.; Liu, S.; Zeng, A.; Lin, J.; Li, K.; Cao, H.; Chen, J.; Huang, X.; Chen, Y.; Yan, F.; et al. 2024. Grounded sam: Assembling open-world models for diverse visual tasks. *arXiv preprint arXiv:2401.14159*.
- Robert, D.; Raguet, H.; and Landrieu, L. 2023. Efficient 3d semantic segmentation with superpoint transformer. In *Proceedings of the IEEE/CVF International Conference on Computer Vision*, 17195–17204.
- Rozenberszki, D.; Litany, O.; and Dai, A. 2024. Unscene3d: Unsupervised 3d instance segmentation for indoor scenes. In *Proceedings of the IEEE/CVF Conference on Computer Vision and Pattern Recognition*, 19957–19967.
- Schult, J.; Engelmann, F.; Hermans, A.; Litany, O.; Tang, S.; and Leibe, B. 2023. Mask3d: Mask transformer for 3d semantic instance segmentation. In *2023 IEEE International Conference on Robotics and Automation (ICRA)*, 8216–8223. IEEE.
- Takmaz, A.; Fedele, E.; Sumner, R. W.; Pollefeys, M.; Tombari, F.; and Engelmann, F. 2023. Openmask3d: Open-vocabulary 3d instance segmentation. *arXiv preprint arXiv:2306.13631*.
- Thomas, H.; Qi, C. R.; Deschaud, J.-E.; Marcotegui, B.; Goulette, F.; and Guibas, L. J. 2019. Kpconv: Flexible and deformable convolution for point clouds. In *Proceedings of the IEEE/CVF international conference on computer vision*, 6411–6420.
- Vu, T.; Kim, K.; Luu, T. M.; Nguyen, T.; and Yoo, C. D. 2022. Softgroup for 3d instance segmentation on point clouds. In *Proceedings of the IEEE/CVF conference on computer vision and pattern recognition*, 2708–2717.
- Wang, W.; Yu, R.; Huang, Q.; and Neumann, U. 2018. Sgpn: Similarity group proposal network for 3d point cloud instance segmentation. In *Proceedings of the IEEE conference on computer vision and pattern recognition*, 2569–2578.
- Wei, M.; Wei, Z.; Zhou, H.; Hu, F.; Si, H.; Chen, Z.; Zhu, Z.; Qiu, J.; Yan, X.; Guo, Y.; et al. 2023. AGConv: Adaptive graph convolution on 3D point clouds. *IEEE Transactions on Pattern Analysis and Machine Intelligence*, 45(8): 9374–9392.
- Wu, X.; Jiang, L.; Wang, P.-S.; Liu, Z.; Liu, X.; Qiao, Y.; Ouyang, W.; He, T.; and Zhao, H. 2024. Point transformer v3: Simpler faster stronger. In *Proceedings of the IEEE/CVF Conference on Computer Vision and Pattern Recognition*, 4840–4851.
- Xu, M.; Ding, R.; Zhao, H.; and Qi, X. 2021. Paconv: Position adaptive convolution with dynamic kernel assembling on point clouds. In *Proceedings of the IEEE/CVF conference on computer vision and pattern recognition*, 3173–3182.

Xu, M.; Yin, X.; Qiu, L.; Liu, Y.; Tong, X.; and Han, X. 2023. Sampro3d: Locating sam prompts in 3d for zero-shot scene segmentation. *arXiv preprint arXiv:2311.17707*.

Xu, W.; Shi, C.; Tu, S.; Zhou, X.; Liang, D.; and Bai, X. 2024. A unified framework for 3d scene understanding. *Advances in Neural Information Processing Systems*, 37: 59468–59490.

Yan, M.; Zhang, J.; Zhu, Y.; and Wang, H. 2024. Maskclustering: View consensus based mask graph clustering for open-vocabulary 3d instance segmentation. In *Proceedings of the IEEE/CVF Conference on Computer Vision and Pattern Recognition*, 28274–28284.

Yang, B.; Wang, J.; Clark, R.; Hu, Q.; Wang, S.; Markham, A.; and Trigoni, N. 2019. Learning object bounding boxes for 3d instance segmentation on point clouds. *Advances in neural information processing systems*, 32.

Yang, J.; Ding, R.; Deng, W.; Wang, Z.; and Qi, X. 2024. Regionplc: Regional point-language contrastive learning for open-world 3d scene understanding. In *Proceedings of the IEEE/CVF conference on computer vision and pattern recognition*, 19823–19832.

Yang, Y.; Wu, X.; He, T.; Zhao, H.; and Liu, X. 2023. Sam3d: Segment anything in 3d scenes. *arXiv preprint arXiv:2306.03908*.

Yeshwanth, C.; Liu, Y.-C.; Nießner, M.; and Dai, A. 2023. Scannet++: A high-fidelity dataset of 3d indoor scenes. In *Proceedings of the IEEE/CVF International Conference on Computer Vision*, 12–22.

Yin, Y.; Liu, Y.; Xiao, Y.; Cohen-Or, D.; Huang, J.; and Chen, B. 2024. Sai3d: Segment any instance in 3d scenes. In *Proceedings of the IEEE/CVF Conference on Computer Vision and Pattern Recognition*, 3292–3302.

Zhai, X.; Mustafa, B.; Kolesnikov, A.; and Beyer, L. 2023. Sigmoid loss for language image pre-training. In *Proceedings of the IEEE/CVF international conference on computer vision*, 11975–11986.

Zhang, Z.; Ding, J.; Jiang, L.; Dai, D.; and Xia, G. 2024. Freepoint: Unsupervised point cloud instance segmentation. In *Proceedings of the IEEE/CVF Conference on Computer Vision and Pattern Recognition*, 28254–28263.

Zhao, H.; Jiang, L.; Jia, J.; Torr, P. H.; and Koltun, V. 2021. Point transformer. In *Proceedings of the IEEE/CVF international conference on computer vision*, 16259–16268.

Zhao, J.; Zhuo, J.; Chen, J.; and Ma, H. 2025. SAM2Object: Consolidating View Consistency via SAM2 for Zero-Shot 3D Instance Segmentation. In *Proceedings of the Computer Vision and Pattern Recognition Conference*, 19325–19334.

Supplementary Material

The supplementary material provides additional details on Related Work, Implementation Details, as well as extended Quantitative and Qualitative Results. Code is available at <https://github.com/anonymouse-ktspqazx/SGS-3D>.

Related Work

Closed-set 3D Segmentation 3D semantic segmentation (Qi et al. 2017a,b; Xu et al. 2021; Qian et al. 2022; Robert, Raguet, and Landrieu 2023) assigns a semantic label to each point in a point cloud, identifying the class of the object it belongs to. In contrast, 3D instance segmentation (Hou, Dai, and Nießner 2019; Yang et al. 2019; Wang et al. 2018; Han et al. 2020; Jiang et al. 2020; Vu et al. 2022; Schult et al. 2023; Ngo, Hua, and Nguyen 2023; Kolodiazny et al. 2024) goes a step further by not only categorizing points but also distinguishing individual object instances, even among those of the same category. Early research primarily focused on utilizing shape features such as normal vectors and curvature to identify object instances (He, Shen, and Van Den Hengel 2021; Wang et al. 2018). With the development of 3D scene datasets and point cloud processing techniques, a variety of deep learning-based point cloud segmentation methods emerged. Methods using convolutional neural networks (Milioto et al. 2019; Xu et al. 2021; Thomas et al. 2019), Transformer architectures (Lai et al. 2022; Zhao et al. 2021; Schult et al. 2023; Wu et al. 2024), and graph neural networks (Wei et al. 2023; Han et al. 2024) have shown significant performance improvements on several benchmark datasets due to their ability to better handle complex point cloud data, gradually becoming the dominant approach in the field. While recent advances in unsupervised learning (Rozenberszki, Litany, and Dai 2024; Zhang et al. 2024) have mitigated annotation dependency by leveraging geometric consistency and self-supervised signals, these methods exhibit limited generalization to unseen categories, as they remain constrained by implicit category biases present in their training data. Traditional closed-set 3D instance segmentation methods, which require labeled data for a fixed set of categories, often suffer substantial performance degradation when applied to open-set environments containing previously unseen object classes.

2D Foundation Models for 3D Segmentation Recent advances in large-scale vision have produced powerful 2D foundation models (Radford et al. 2021; Jia et al. 2021; Kirillov et al. 2023; Liu et al. 2024), which exhibit remarkable generalization and robustness. These models have opened new avenues for 3D scene segmentation and understanding.

Based on CLIP (Radford et al. 2021), some methods (Peng et al. 2023; Ding et al. 2023; Hegde, Valanarasu, and Patel 2023; Yang et al. 2024) typically construct point-wise feature representations for 3D point clouds and align them with arbitrary text queries to enable open-vocabulary 3D segmentation. For instance, OpenScene (Peng et al. 2023) employs feature distillation to transfer knowledge from 2D vision-language models, while PLA (Ding et al. 2023) generates scene-level textual captions to bridge 3D geometric contexts and semantic descriptions. However, these CLIP-

based methods often struggle with the 2D-3D domain gap inherent to their pre-training.

A distinct approach utilizes the Segment Anything Model (SAM) (Kirillov et al. 2023), which is trained on over a billion masks and demonstrates strong zero-shot generalization to novel scenes by generating high-quality 2D instance masks. Capitalizing on this, many methods attempt to lift these 2D masks into the 3D space to obtain object instances.

Some methods (Yang et al. 2023; Lu et al. 2023b; Yan et al. 2024) primarily operate by establishing relationships and consistency directly among the projected 2D mask segments onto the 3D point cloud, subsequently merging associated mask fragments to form coherent 3D object instances. Based on 2D masks generated by SAM, some approaches (Xu et al. 2023; Nguyen et al. 2024; Yin et al. 2024; Guo et al. 2024) additionally introduce 3D geometric primitives (e.g., superpoints) as fundamental units to guide instance formation. SAM-graph (Guo et al. 2024) constructs a superpoint graph and employs a Graph Neural Network (GNN) to refine the segmentation results. SAI3D (Yin et al. 2024) leverages SAM masks to quantify the affinity scores of superpoints and progressively merge them. Open3DIS (Nguyen et al. 2024) maps the 2D masks into superpoint regions, guiding the merging process of 3D instances. SAM2Object (Zhao et al. 2025) leverages cross-frame tracking of 3D object instances via SAM2 to obtain 2D masks for graph clustering. In contrast, our approach prioritizes semantic clusters derived from projected 2D instance masks and employs 3D geometric primitives as auxiliary support to promote their expansion and subsequent consolidation into high-fidelity 3D instances.

Implementation Details

Baselines We compare our method against a comprehensive set of recent and classical baselines for class-agnostic 3D instance segmentation. We group these baselines into two main categories: *training-dependent* and *training-free* methods.

Training-dependent methods require fine-tuning or training on specific 3D datasets. In this category, we include UnScene3D (Rozenberszki, Litany, and Dai 2024), which leverages DINO features, as well as Segment3D (Huang et al. 2024) and SAM-graph (Guo et al. 2024), both of which build upon the Segment Anything Model (SAM).

Training-free methods operate in a zero-shot manner without any 3D data training. This category is further divided into traditional algorithms and modern 2D-to-3D lifting approaches. Traditional algorithms rely on low-level geometric and color attributes. We report results from the density-based clustering method HDBSCAN (McInnes and Healy 2017) and the graph-based Felzenszwalb’s method (Felzenszwalb 2004). 2D-to-3D Lifting methods represent the current state-of-the-art among training-free approaches, lifting segmentations from 2D Vision Foundation Models (VFMs) to the 3D domain. We compare against SAM3D (Yang et al. 2023), SAI3D (Yin et al. 2024), Open3DIS (Nguyen et al. 2024), and SAM2Object (Zhao et al. 2025), which utilize various VFMs like SAM (Kirillov et al. 2023),

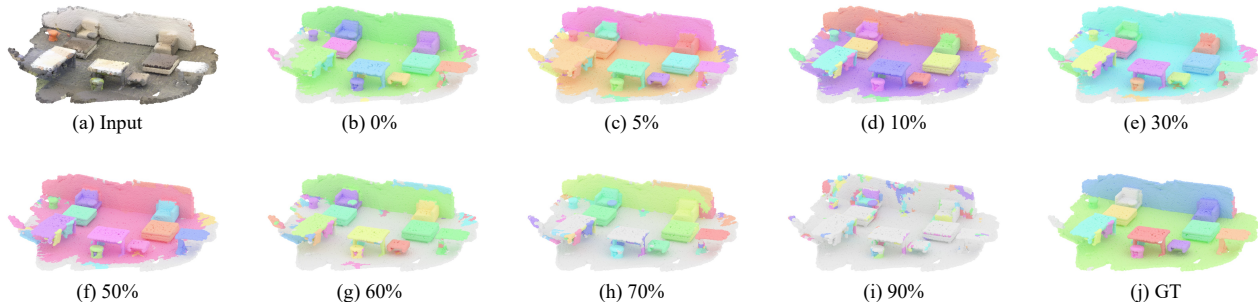


Figure 9: Visualization of qualitative segmentation results under varying occlusion levels. Our method maintains competitive performance even under extreme occlusion of 50%.

Grounded-SAM (GD-SAM) (Ren et al. 2024), and SAM2 (Ravi et al. 2024).

2D Mask Generation Our 2D mask generation leverages Grounding-DINO (Liu et al. 2024) and SAM (Kirillov et al. 2023) (ViT-H variant) for targeted mask proposals. To achieve this, we first construct a text prompt by concatenating the official class names of the target dataset (e.g., the 200 classes for ScanNet200). Grounding-DINO uses this prompt to detect relevant objects, and we retain bounding boxes with a confidence score above 0.4. These boxes are then fed to SAM to generate the initial mask set $\mathcal{M}_{2D,t}$. As validated in Table 5, this GD-SAM approach is superior, achieving 34.3% mAP on ScanNet200. This significantly outperforms using the original SAM directly (32.3% mAP), confirming that our targeted strategy provides a more accurate foundation for the SGS-3D pipeline.

Superpoint Generation Our pipeline begins by partitioning the input 3D data into superpoints. The method for this process is chosen based on the input data format. Following (Yin et al. 2024; Guo et al. 2024), for indoor datasets represented as meshes (ScanNet200 and ScanNet++), we utilize the official segmentation tool in (Dai et al. 2017). This function segments the mesh by clustering vertices based on a distance threshold ($kThresh$) and subsequently merges segments smaller than a minimum vertex count ($segMinVerts$). For the ScanNet200 dataset, we use the pre-computed segmentations provided, which were generated with $kThresh$ set to 0.01 and $segMinVerts$ to 20. For the denser ScanNet++ dataset, we re-run the segmenter with adjusted parameters, setting $kThresh$ to 0.2 and $segMinVerts$ to 500 to obtain appropriately sized superpoints. For the outdoor unstructured point clouds of KITTI-360, we employ the partitioning method from (Landrieu and Simonovsky 2018). This approach solves a global energy minimization problem to generate geometrically coherent superpoints. For this process, we adopt the default hyperparameters as specified in (Robert, Raguet, and Landrieu 2023).

Simulated Occlusion Experiments To rigorously evaluate the robustness of SGS-3D against occlusions, we de-

signed a controlled experiment using a patch-dropping protocol, inspired by (Naseer et al. 2021; Boudjoghra et al. 2024). We systematically simulate partial occlusions and assess their impact on the final segmentation performance.

Our simulation directly targets the 2D instance masks generated by the foundation model. For each foreground mask, we randomly discard a certain percentage (from 5% to 90%) of its pixels by setting them to zero. This effectively creates "holes" or partial views of the object within that specific 2D mask. A key aspect of this protocol is that it focuses exclusively on semantically meaningful foreground objects. Since our pipeline's initial steps naturally disregard large background structures like walls and floors, this simulation accurately models the challenging real-world scenario where key objects of interest are partially obscured, rather than simulating random occlusions anywhere in the image. Figure 9 provides a visual example of a scene under varying levels of simulated foreground occlusion.

The quantitative results, presented in Table 7, demonstrate the high resilience of our pipeline. Performance remains remarkably stable with almost no degradation for occlusion levels up to 30%. Even under the extreme condition of 50% foreground occlusion, the mAP is still a competitive 29.6, indicating that our system can produce meaningful segmentations from severely incomplete 2D semantic guidance. As expected, performance degrades gracefully as the occlusion level increases further. This stability stems from SGS-3D's core ability to aggregate partial information from multiple views and its reliance on strong 3D geometric principles during the splitting and growing phases, which can effectively compensate for corrupted or incomplete semantic cues from any single view.

Additional Quantitative Results

Quantitative Comparison with Closed-Set Method Following (Guo et al. 2024), We also compare our method against the supervised method Mask3D (Schult et al. 2023), to evaluate its generalization ability. As reported in Table 8, Mask3D achieves excellent results on the ScanNet200 validation set when trained on its corresponding training

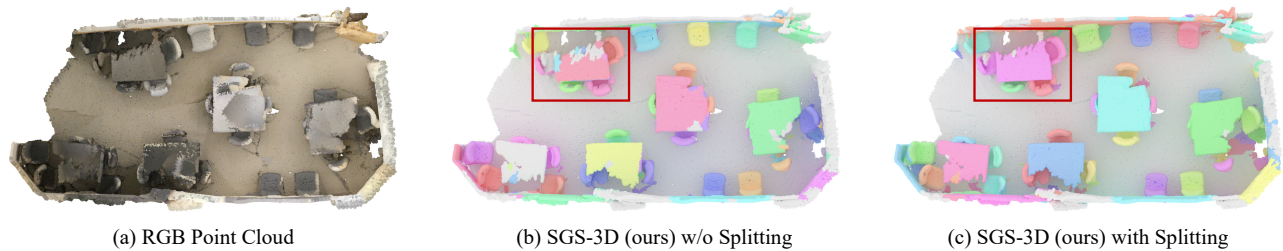


Figure 10: Qualitative analysis of Spatial Continuity Splitting (SCP). Without the SCP step, the ambiguous initial mask erroneously merges the chair and table. This flawed seed subsequently hinders the "growing" process, resulting in an incomplete and incorrect instance (b). By incorporating our SCP step, the initial mask is correctly split based on geometric contiguity. This high-purity seed enables our "split-then-grow" strategy to produce a complete and high-fidelity 3D instance segmentation (c).

		Training Data	mAP	AP ₅₀	AP ₂₅
ScanNet200	Mask3D	GT of ScanNet200	53.3	71.9	81.6
	Mask3D	GT of ScanNetV2	45.1	62.6	70.5
	Ours	-(Zero-shot)	34.3	51.3	64.6
ScanNet++	Mask3D	GT of ScanNet200	4.6	10.5	22.9
	Mask3D	GT of ScanNetV2	3.7	7.9	15.6
	Ours	-(Zero-shot)	23.7	39.6	54.3
KITTI-360	Mask3D	GT of ScanNet200	0.2	0.9	7.0
	Mask3D	GT of ScanNetV2	0.3	1.0	8.0
	Ours	-(Zero-shot)	32.9	43.7	53.4

Table 8: Comparison with Mask3D. Mask3D achieves superior performance on its native ScanNet200 test set but fails to generalize to new domains.

set, outperforming our approach. However, its performance drops significantly when the same model is applied to other datasets. On ScanNet++, which uses a different sensor for data acquisition, the mAP of the ScanNet200-trained model falls from 53.3% to 4.6%. This generalization issue is even more pronounced on the outdoor KITTI-360 dataset, where Mask3D's performance becomes extremely poor. In contrast, our training-free SGS-3D delivers stable and competitive performance across all three diverse benchmarks. This comparison clearly highlights the strong zero-shot generalization capability of our approach, which avoids the dataset-specific overfitting inherent in supervised methods.

Occlusion-Aware Mapping To further evaluate the necessity and superiority of our viewing visibility verification for precise occlusion detection, as detailed in the main paper's Point-Image Mapping section, we conducted a series of ablation studies. We compared three distinct point-to-pixel mapping strategies and assessed their impact on the final 3D instance segmentation accuracy on both indoor (ScanNet200) and outdoor (KITTI-360) datasets. The strategies include Naive Projection, which considers any point with a positive depth value ($z > 0$) as visible, thereby ignoring all occlusions; Min-Depth Filtering, which only deems the point with the minimum depth at each pixel location as visible; and our proposed occlusion-aware method, which leverages a constructed depth buffer and a tolerance threshold.

As shown in Table 9, establishing an inaccurate point-

Method	ScanNet200			KITTI-360		
	mAP	AP ₅₀	AP ₂₅	mAP	AP ₅₀	AP ₂₅
<i>traditional algorithm</i>						
HDBSCAN	2.9	8.2	33.1	9.3	18.9	39.6
<i>ours setting</i>						
Naive Projection	15.8	26.5	40.6	5.1	8.4	14.6
Min-Depth Filtering	17.8	29.7	45.4	7.2	12.2	20.7
Occlusion-Aware	30.5	47.2	62.2	32.9	43.7	53.4

Table 9: Ablation study of viewing visibility verification effectiveness on indoor and outdoor dataset. Without accurate visibility mapping, 2D-lifting-3D based paradigm is even worse than traditional clustering algorithm, which shows the effectiveness of our method.

to-pixel correspondence severely undermines the fidelity of the 2D-to-3D lifting process, leading to a catastrophic drop in 3D instance segmentation performance. This detrimental effect is particularly pronounced in the complex outdoor scenes of KITTI-360, where the mAP plummets to a mere 7.2% with Min-Depth Filtering. This result is even worse than that of the traditional HDBSCAN clustering algorithm (9.3% mAP). In contrast, our occlusion-aware mapping strategy achieves an mAP of 32.9% which serves as the foundation for achieving high-fidelity 3D instance segmentation.

The ablation experiment about τ_{vis} is shown in the Table 10. We choose 0.1 as the default value.

τ_{vis}	0.01	0.05	0.1	0.15	0.2
mAP	29.4	33.5	34.3	32.8	31.6

Table 10: Ablation of depth congruence tolerance τ_{vis} .

Ablation on the Parameter of Splitting As introduced in Section 3.3.1, our Spatial Continuity Splitting (SCP) step refines the initial 3D semantic masks by addressing instances where spatially separate objects are erroneously merged due to their similar appearance, and further separates potential semantic noise (see Figure 10 (b)-(c)). For this process, we apply the HDBSCAN (Campello, Moulavi, and Sander

μ	mAP	AP ₅₀	AP ₂₅
-	29.7	45.2	58.9
10	32.9	49.7	63.6
20	34.1	51.0	64.4
30	34.3	51.3	64.6
40	34.2	50.7	63.8
50	30.4	46.5	59.5

Table 11: Ablation study of the min cluster size μ in indoor scene.

Image Proportion	30%	25%	20%	15%	10%
mAP	23.2	31.6	32.9	28.3	24.5

Table 12: Ablation of image proportion on KITTI-360 dataset.

2013) algorithm to each 3D semantic mask, using the 3D point coordinates for clustering. This partitions each mask into one or more dense, spatially contiguous clusters. Each resulting dense cluster is then treated as a new, more refined semantic-geometric seed ($\mathcal{M}_{seed,t}$). In our hyperparameter ablation study in Tab 11, we achieved overall best results when applying HDBSCAN with the min cluster size μ of 30 for the indoor dataset and μ of 150 for the outdoor dataset.

Analysis of Overlap and Input Image Number The effectiveness of a progressive IoU threshold for the multi-view merging stage has been validated in prior work (Yin et al. 2024; Zhao et al. 2025), as it generally improves accuracy over using a single, fixed threshold. In our experiments, we empirically set the sequence of overlap thresholds to [0.7, 0.6, 0.5, 0.4, 0.3] for ScanNet200 and [0.8, 0.7, 0.6] for ScanNet++.

However, we observed that this progressive strategy provided minimal benefit for the outdoor KITTI-360 dataset, yielding results nearly identical to those from a single fixed threshold. An examination of the datasets reveals a likely cause: outdoor scenes in KITTI-360 contain significantly fewer image frames per scene compared to indoor datasets. This is because the outdoor data is captured from a moving vehicle, in contrast to the dense views achievable with a handheld camera indoors. Under these sparser view conditions, a progressive IoU threshold loses its discriminative power.

Instead, we found that performance on KITTI-360 is highly sensitive to the proportion of input images used. As reported in Table 12, both too few and too many input images lead to a sharp decline in accuracy. This trend is more pronounced than the one observed on indoor datasets (see Table 4 in the main paper). Consequently, for our experiments on KITTI-360, we set the input image proportion to 20% and use a fixed merging threshold of 0.2 as our default configuration.

Open-Set Semantic Application Details As introduced in the main paper, the high-quality, class-agnostic instance proposals generated by SGS-3D serve as an excellent foun-

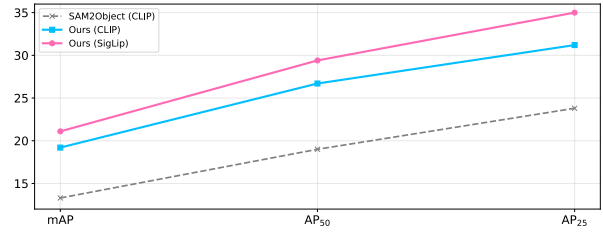


Figure 11: Performance comparison of SGS-3D (ours) and SAM2Object (Zhao et al. 2025) on the ScanNet200 dataset for semantic instance segmentation.

ation for open-vocabulary tasks. Here, we detail the procedure used to assign semantic labels to these proposals, enabling applications like text-based object search.

The core of our method is a visibility-weighted feature aggregation strategy. Following prior work (Takmaz et al. 2023; Nguyen et al. 2024), we compute a representative feature for each 3D instance proposal by aggregating information from 2D views. For the feature extraction, we employ SigLIP (Zhai et al. 2023), a recent vision-language model. We chose SigLIP over the more traditional CLIP as its training objective is better aligned with zero-shot tasks, leading to stronger and more robust performance in open-vocabulary recognition. As illustrated in Figure 11, this choice is empirically validated, with SigLIP consistently outperforming CLIP and widening the performance gap against baselines like SAM2Object (Zhao et al. 2025). This entire process directly benefits from the accurate, occlusion-aware point-image mapping established in Section 3.1 of our main paper.

For each input image I_t , we first extract dense pixel-wise features using the SigLIP image encoder, resulting in a feature map $\mathbf{F}_t^{\text{SigLIP}}$. Then, for every 3D point p_i in the scene, we identify the set of views $\mathcal{T}_i = \{t \mid \mathcal{V}_t(i) = 1\}$ where it is visible. The 3D feature for point p_i , denoted \mathbf{f}_i^{3D} , is computed by averaging its corresponding 2D features across all these visible views:

$$\mathbf{f}_i^{3D} = \frac{1}{|\mathcal{T}_i|} \sum_{t \in \mathcal{T}_i} \mathbf{F}_t^{\text{SigLIP}}(\pi(p_i, I_t)) \quad (6)$$

where $\pi(p_i, I_t)$ is the projection of point p_i onto image I_t . This ensures that points consistently observed across many views have a more robust and stable feature representation.

With 3D features established for every point, we then compute a single, representative feature vector $\mathbf{F}_k^{\text{prop}}$ for each of our final 3D instance proposals M_k . This is achieved by averaging the 3D features of all points within that proposal:

$$\mathbf{F}_k^{\text{prop}} = \frac{1}{|M_k|} \sum_{p_i \in M_k} \mathbf{f}_i^{3D} \quad (7)$$

where $|M_k|$ is the number of points in the proposal M_k .

Finally, to match a given text query ρ (e.g., "a square table"), we encode it into a text embedding \mathbf{e}_ρ using the SigLIP text encoder. The relevance score $s_{k,\rho}$ between the text and each proposal M_k is the cosine similarity between

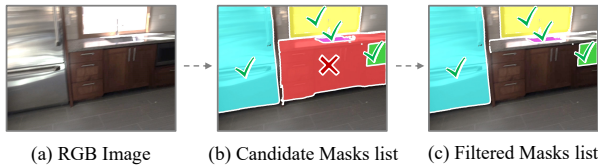


Figure 12: An example of filtering 2D candidate mask that incorrectly merges two distinct objects ('kitchen counter' and 'kitchen cabinet').

their respective feature vectors:

$$s_{k,\rho} = \cos(\mathbf{F}_k^{\text{prop}}, \mathbf{e}_\rho) \quad (8)$$

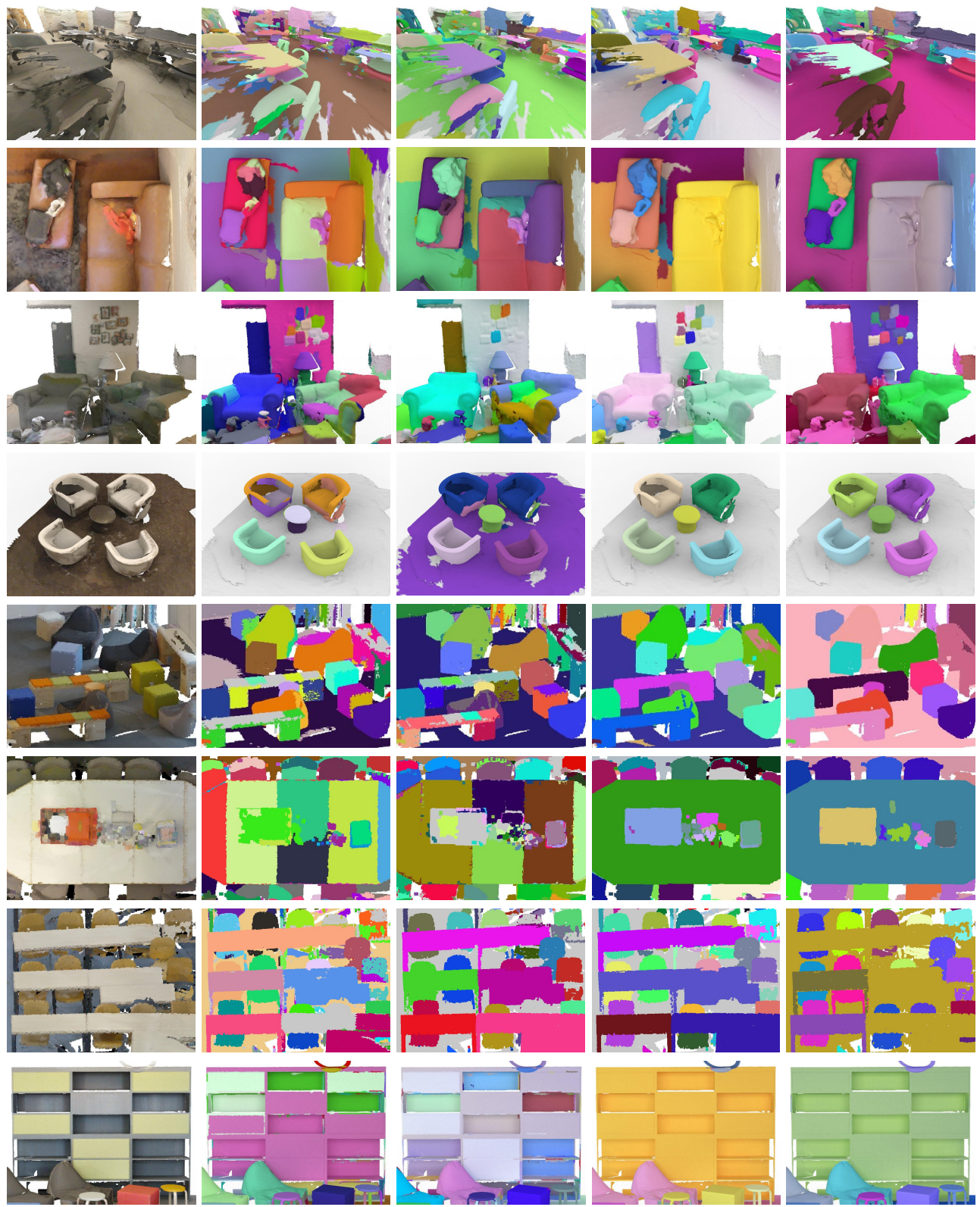
The proposal with the highest score is identified as the best match for the text query.

Additional Qualitative Results

Robustness Against Erroneous Masks Our Co-occurrence Mask Filtering (CMF) module serves as a critical pre-processing step, designed to identify and prune ambiguous or incorrect 2D masks before they are lifted to 3D. This prevents the propagation of semantic errors that would otherwise corrupt the subsequent instance generation process. Figure 12 provides a qualitative example of its effectiveness.

In the figure, we observe an initial mask proposal from the 2D foundation model that erroneously merges two distinct objects: a 'kitchen counter' and an adjacent 'kitchen cabinet'. Although this mask might appear plausible in a single 2D view, it is inconsistent from a 3D geometric standpoint. Our CMF module quantifies this inconsistency by calculating a co-occurrence score (as defined in Eq. 4) for each mask, which measures its average visibility agreement with all other candidate masks across multiple views. The erroneous 'counter-cabinet' mask receives a low co-occurrence score and is subsequently removed from the candidate list. This is because it fails to find consistent support from other views, which would correctly segment either the counter or the cabinet, but not both as a single entity. The importance of this filtering mechanism is quantitatively validated in our ablation study (Table 2), where the inclusion of CMF provides a substantial boost in segmentation accuracy.

More Visualization of 3D Instance Segmentation Additional qualitative segmentation results of SGS-3D for indoor and outdoor scenes are presented in Figure 13 and Figure 14, respectively.



Input

SAM3D

Open3DIS

Ours

Ground Truth

Figure 13: Additional visual results of 3D instance segmentation on indoor dataset (Dai et al. 2017) and (Yeshwanth et al. 2023).

